ACS APPLIED ELECTRONIC MATERIALS

pubs.acs.org/acsaelm Article

High-Performance Conformal Thermoelectric Generator for Environmental Monitoring

Yining Feng,* Kazuaki Yazawa, and Na Lu

Cite This: *ACS Appl. Electron. Mater.* 2022, 4, 197−205 Read Online

ACCESS | Metrics & More | Article Recommendations

ABSTRACT: A continuous underground pipeline monitoring system is needed to avoid energy waste or pipeline explosions and minimize the negative environmental impact. Thermoelectric-powered Internet of things (IoT) sensors can be a promising solution due to reliable power sources supplied by thermoelectric generators to scavenge the wasted heat through the pipeline surface. Conformal thermoelectric generators (cTEGs) are suitable for pipeline applications; however, the current study is mainly focused on harvesting body heat, which is not suitable for piping systems because of the different thermal path. Here we designed and fabricated a film-based cTEG on a roll-to-roll manufacturing platform using an electrothermal model to achieve an optimized device structure and performance. The unique design of this cTEG device provides the capability of scavenging mid- to low-grade waste heat, which is the most common wasted heat source for underground pipeline systems. The proposed device fabrication method combines bulk TE elements with a flexible printed circuit board to maximize the power output and minimize the cost. The resulting power output density of a cTEG integrated with four pairs of p−n junctions is 1.26 mW/m^2 at a temperature difference of 50 °C, which is 2 times higher than the value reported in the current literature. This study provides a potential pathway for using TEGs as energy sources for powering underground pipeline monitoring systems in a cost-effective way for real applications.

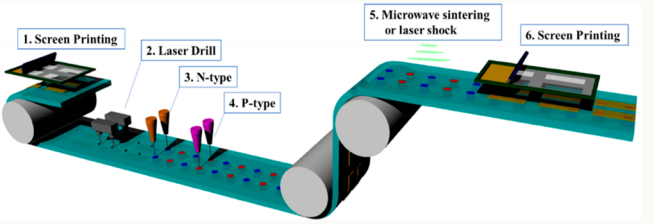

KEYWORDS: *conformal thermoelectric generator, internet of things, energy harvesting, environmental monitoring, smart infrastructure, thermoelectricity*

INTRODUCTION

Underground pipelines are conventionally considered to be low-risk infrastructure because the reported incidents are relatively rare. however, they often have devastating consequences when incidents occur. In 2018, a steam pipe exploded in downtown New York City, which caused severe human injuries and property damage. Also, the products released from underground pipes can be harmful to the environment.[1] Thus, a continuous underground pipeline monitoring system is needed to solve the problems. Internet of Things (IoT) sensors with integrated wireless sensor networks (WSNs) play a critical role in monitoring underground pipelines. As the demand for IoT sensors increases, the source of powering these sensors becomes a vital issue. A battery is the most commonly used power source, which requires extra labor and cost for replacement and maintenance. In addition, it is extremely cumbersome for the battery-powered IoT to be applied in remote areas or areas with limited access. To overcome these limitations, researchers have explored several novel methods using renewable energy as the power sources such as solar energy,[2] piezoelectric energy harvester, etc.[3] However, due to the limitations of working conditions and cost, these renewable energy sources are not always suitable for WSNs and portable electronics. It is evident that thermoelectric (TE) technology is an important advancement in the renewable energy field, due to its ability to directly convert heat into electricity for power generation via the Seebeck effect.[4−6] It can play a crucial role in sustainable electricity production, since nearly 60% of the primary energy source worldwide is wasted in the form of heat. Additionally, thermoelectric generators (TEGs) have the advantages of low maintenance, no moving parts, and ease of installation.

Despite recent advances in TE technology, the potential effects of TE devices for power generation are limited. The main challenge lies in the rigid device geometry and complicated fabrication process. Conventional TEG devices are platelike and rigid, which are unable to be used for fully exploiting thermal gradients (ΔT) from curved or nonplanar surfaces, as most heat sources have nonplanar surfaces or

Received: September 27, 2021
Accepted: January 4, 2022
Published: January 13, 2022

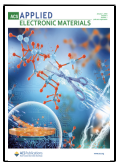

spatial restrictions. In addition, the current production of TEG devices involves a complicated fabrication process with many discrete steps and rigid substrates. As such, the cost of fabrication and packaging of TEG devices counts for more than 70% of the total cost. Despite the numerous efforts and advancement of TE technology at a materials level, the inefficient device fabrication process has unfortunately not been well addressed in the TE community.

Research has been conducted since 2001 on the fabrication methods for conformal TEGs (cTEG).[7] There are several different fabrication techniques, such as a lift-off process,[8,9] a flash evaporation method,[10,11] photolithography and etching techniques,[12−14] thermal evaporation,[15] nanomaterials,[16−19] sputtering techniques,[20−22] screen printing,[23−27] dispenser printing,[28−31] and inkjet printing.[32−35] Among all these methods, printing technologies are the most commonly used techniques for cTEG device fabrication. However, the current existing printing technologies are limited by the ink viscosity, printing thickness, binders, etc.

The previous studies on polymer-based TEG modules have indicated a low performance due to the TE legs being shorter than the optimum. To overcome the challenges for traditional printing technologies, we propose a hybrid cTEG fabrication method that combines bulk TE elements with a flexible printed circuit board. The electrothermal modeling used in this work provides the capability of maximum performance design for any dimension constraints. Also, the proposed fabrication process can be easily transferred to a roll-to-roll platform that reduces the manufacturing costs, which is another major limitation for the adoption of thermoelectric technology. The testing system is built by a thermal path similar to that of the real underground pipeline application, which provides reliable results for the study.

CO-OPTIMIZATION OF TEG DEVICE ELECTROTHERMAL PROPERTIES

The TEG device performance (power output and efficiency) relies on the material's figure of merit (zT) enhancement and it is also affected by the efficiency of heat transfer from the heat source to the heat sink. It works as a whole energy conversion system that needs to be electrically and thermally optimized. Yazawa et al. has developed electrothermal co-optimized TEG modeling that can be used as a guideline for this study.[36] There are two ways to look into the performance of TEG: either maximum output power or highest efficiency. This depends on the different applications. On the one hand, for power generation where the heat source is continuous, unlimited, and essentially free or has a negligibly low cost, the maximum power output is more important than efficiency. On the other hand, for a limited and expensive heat source, efficiency must be weighted against sacrificing some portion of the power output. For modeling optimization, the highest output corresponds to the highest power delivered to a load. The highest efficiency corresponds to the highest ratio of electrical power delivered to load to the amount of heat flux from a hot reservoir to a cold reservoir.

As the electrical and thermal properties are interdependent, it is important to analyze the electrical current flow and heat flow simultaneously. A system diagram that includes both thermal resistance and the electrical circuit is shown in Figure 1.

The equations at the two nodes are based on energy conservation; T_h and T_c are the temperatures at the hot and

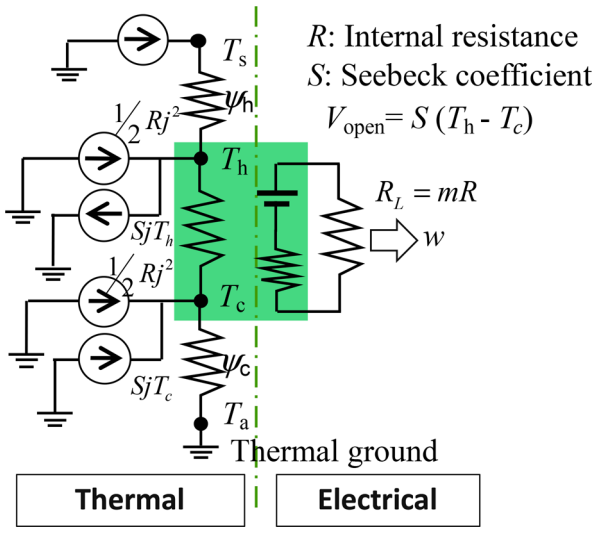

Figure 1. Electrothermal resistance network model. The green block represents the thermoelectric material (leg), and the upper and lower sides of the region represent the electrical and thermal contacts. ψ_h and ψ_c are the thermal resistances for the heat transfer on the hot side and cold sides, respectively. q_h is the heat flux supplied by the hot reservoir at temperature T_s (fixed). q_c is the heat flux that flows into the cold reservoir being reduced from q_h depending on the energy conversion efficiency.[37]

cold sides of the thermoelectric legs, respectively. Heat flux applied to the thermoelectric leg (W/m^2) and the rejected heat flux on the cold side (W/m^2) are found to be

$$q_h = \frac{\beta}{d}(T_h - T_c) + SIT_h - I^2R/2 \quad (1)$$

$$q_c = \frac{\beta}{d}(T_h - T_c) + SIT_c + I^2R/2 \quad (2)$$

where β is the thermal conductivity (W/(m K)), S is the Seebeck coefficient (V/K), I is the electrical current per unit (A/m^2), and $R = \frac{d}{\sigma}$ is the internal electrical resistance with unit cross-sectional area (Ω m^2). Both hot and cold junctions dissipate half of the total power as the Joule heating happens in the TE leg. The output power delivered to the load per unit area of the heat source w (W/m^2) is found to be[36]

$$w = I^2mR = \frac{m\sigma S^2}{(1+m)^2 d}(T_h - T_c)^2 \quad (3)$$

where $w = q_h - q_c$ by energy conservation, σ is the electrical conductivity of the leg, and m is the ratio of the internal resistance to the external load resistance, i.e. $R_L = mR$.

The maximum power output as a function of T_s and T_a can be calculated as[36]

$$w = \frac{mZ}{\alpha^2(1+m)^2}\frac{\beta}{d_{opt}}(T_s - T_a)^2 \quad (4)$$

where α is the asymmetric factor (dimensionless) defined as $\alpha = (T_s - T_a)/(T_h - T_c)$ and d_{opt} is the optimum leg length. Z is the material's figure of merit with dimensions of 1/K consisting of the intrinsic material property Seebeck coefficient S (V/K), the thermal conductivity β (W/(m K)), and electrical conductivity σ (1/(Ω m)) as $Z = \sigma S^2/\beta$ (1/K). If the TE legs are thin and long, the system can hold a large temperature difference. However, the electrical resistance increases for long

https://doi.org/10.1021/acsaelm.1c00922
ACS Appl. Electron. Mater. 2022, 4, 197−205

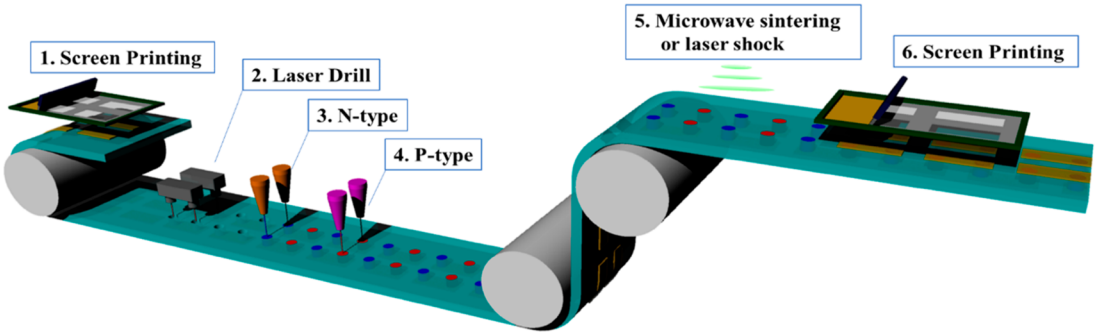

Figure 2. Schematic of the proposed roll-to-roll production line of a conformal thermoelectric generator (cTEG).

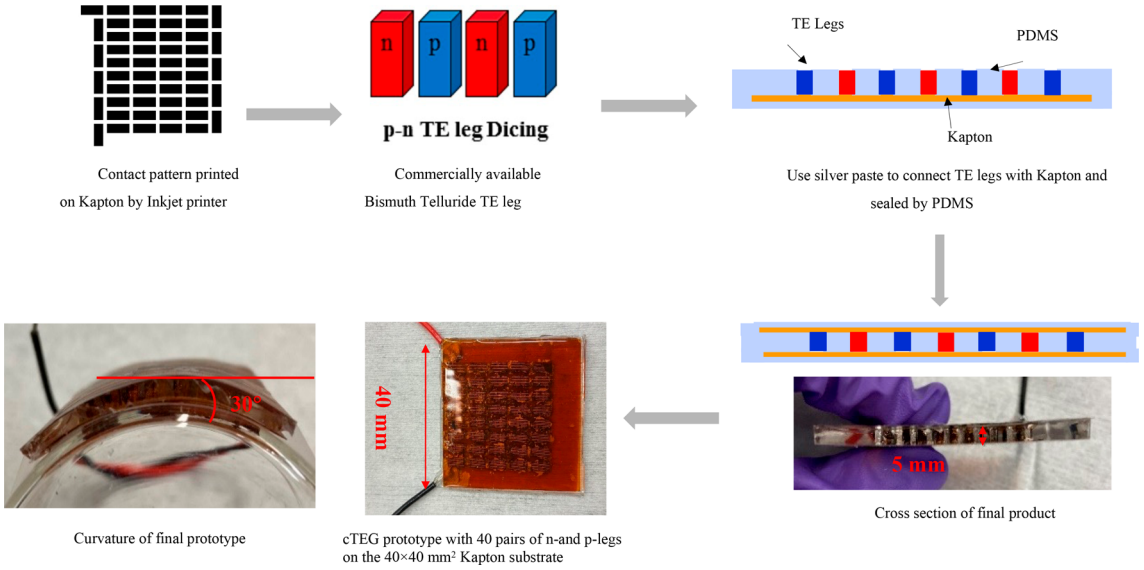

Figure 3. Fabrication process and cTEG prototype. Simplified fabrication process of cTEG: (1) inkjet printing of the silver pattern by inkjet printing; (2) use of the commercially available bismuth telluride as TE legs; (3) use of silver paste to connect the bulk TE elements with Kapton and with subsequent filling of the hole and sealing by PDMS; (4, 5) images of the cTEG prototype with 40 pairs of n-and p-legs on a 40 × 40 mm^2 Kapton substrate. The cross section shows a whole device thickness of 5 mm.

legs and the power output will decrease. Thus, there is an optimized leg length that yields a maximum power output, where the ratio of internal and external resistance $m = \sqrt{1 + zT}$.[37] This relation is found when the temperature reservoirs T_s and T_a are given while T_h and T_c are variables. In realistic cases, the terminal temperatures of thermoelectric legs are variables by the design of external thermal resistances and/or thermoelectric legs. To clarify, impedance matching with $m = 1$ for maximum power output only happens when T_h and T_c are given and fixed. An assumption has been made that the zT value is constant across the study cases due to the limited temperature range in this application. The real deviation of the temperature-dependent zT value consisting of three material properties are process-dependent and not yet known. Therefore, this modeling design took the liberty to make the analyses simpler.

CONFORMAL THERMOELECTRIC DEVICE FABRICATION

Experiment. Figure 2 shows the schematic of a conceptual production line and the process for cTEG using several microdeposition processes on a roll-to-roll platform, which include the following (1) The top metal contact layers (shown as yellow color) are deposited onto a PDMS film substrate (shown in green) using screen-printing techniques with silver ink, and a curing process follows to ensure that the electrical conductance is secured. (2) Vertical micropits are created on the polymer substrates using a pulsed laser irradiation system, (3, 4) Vertical microhollows are filled with p- or n-type TE materials, respectively, in a staggered pattern. Pipet dispensing systems or similar techniques are used, while the TE materials are prepared as nanoparticles for deposition. (5) p- and n-type TE materials deposited in the pits are sintered using a pulsed laser or microwave for *in situ* crystallization with minimal thermal damage to the polymers, followed by (6) screen-printing the top layer metal contacts to allow the generated electrical current flow through the entire cTEG module. The printed electrode ink is then cured at 90 °C for 2 h. Finally, the device is laminated by a top side substrate such as a polyimide film. The roll-to-roll process allows infinitely continuous electrical circuitry, and it can be cut at any desired length to make the sheetlike device.

To avoid thermal losses, it is important to use highly insulating polymers (i.e., PDMS) as the gap-filling materials between p-type and n-type legs. This structure also allows large strain and deformation. Hence, this device design is expected to provide good energy conversion efficiency and mechanical conformability. The numbers of p−n pairs are determined by

https://doi.org/10.1021/acsaelm.1c00922
ACS Appl. Electron. Mater. 2022, 4, 197−205

the required power output specific to the application. The lengths of p and n legs and the widths and thicknesses of contacts are designed to maximize the power output on the basis of both the material's properties and the heat transfer efficiency on the hot and cold boundaries.

Before all of the above technologies were fully implemented into a large-scale cTEG production, a simplified fabrication process was utilized in this study and the performance tests were conducted on the fabricated sample to test the feasibility of the proposed method.

Figure 3 shows the tested sample of a cTEG prototype using solid TE legs available commercially with a flexible polyimide substrate and PDMS as filling materials. Both n- and p-type Bi_2Te_3 (Seebeck coeffcicent 201 μV/K, electrical conductivity 1×10^{-3} S/cm, thermal conductivity 1.5×10^{-2} W/(cm K)) cubic legs have a size of 1 × 1 × 3.5 mm. The prototype fabrication process includes the following. (1) The contact pattern was designed by Adobe Illustrator, as shown in Figure 3. Silver ink (NovaCentrix JS-A101A) was used as conducting contacts for the prototype. The designed pattern with a size of 1.5 × 3 mm was printed on the Kapton substrate with a thickness of 273 μm by using an inkjet printer (FUJIFILM Dimatix DMP-2850) with different fill factor designs. (2) The printed silver ink was cured at 90 °C for 2 h to ensure high electrical conductivity. To achieve electrical connections, the entire printed pattern was designed to make a series connection. (3) A high-performance silver paste (PELCO, No. 16047) was used for soldering n- and p-type legs and connection wires on the top and bottom as-patterned Kapton substrates. (4) The electrical connections for the entire TE module were checked by connecting a voltmeter to two wires. (5) Finally, PDMS (Dow Corning SLYGARD 184 kit) was used as the filling material for the TE module. The as-fabricated TE module was placed on a hot plate, and then well-mixed PDMS with a curing agent was poured into a mold and cured for 2 h at 80 °C. Figure 3 shows the fabricated prototype of a TE module that includes 40 pairs of n- and p-type legs on a 40 mm × 40 mm area. The total thickness of the TE module is 5 mm, as designed by simulation results.

Figure 3 shows the good mechanical flexibility of the fabricated TE module. The TE module was attached on the outside of a laboratory beaker, with a curve angle of approximately 30°. As the cTEG will be used as a power source for an underground pipeline, the curvature with a 30° angle is suitable for this specific application.

Testing Setup. The overall view of the testing setup is shown in Figure 4a. The apparatus externally creates the temperature difference across the as-fabricated cTEG module by the counterdirection of two water flows. Water chillers supply deionized water flows to the cold and hot sides, where the temperatures are controlled within ±0.1 °C accuracy (Fisher Scientific ISOTEMP 250LCU).[37] The cold side is fixed at 5 °C during this experiment. The hot side increases from 5 °C up to 55 °C. The flow meters (FTB333D, Omega Engineering) measure the water flows from the chiller to testing bed with ±6% accuracy for a 0.2−2 mL/min range. The amount of heat loss during the measurement is considerably smaller in comparison to the main heat flow.

Figure 4b shows a side view of the sample stage where the TE module is placed between copper plates. Thermal interface grease (OMEGA THERM 201) is used on the top and bottom sides of the TE module to maintain reasonably good thermal contacts. In order to compare the results with those of other studies, the measured TE modules contain four pairs of TE legs in a 40 mm × 40 mm area.

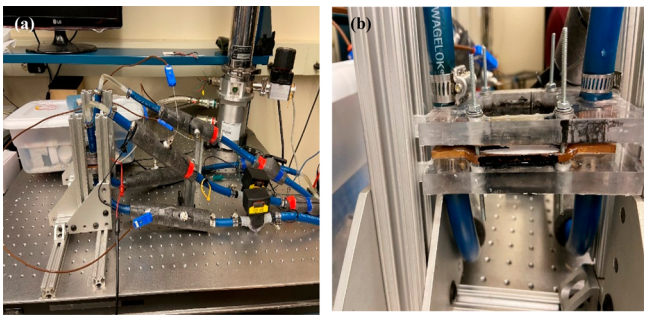

Figure 4. (a) Overall view of the test setup with two water flows controlled by chillers. The cold side is set at 5 °C, and the hot side is changed from 5 to 55 °C. The water flow rate is recorded by a flow meter that is mounted on the tube. (b) Sample stage for the cTEG device. The cTEG device is placed between two copper plates with thermal interface grease on both sides.

RESULTS AND DISCUSSION

The temperature boundary conditions on the outside of the cTEG module are controlled by the water flow. Due to the heat loss from the heat reservoirs to the cTEG module, temperature gradients are involved on the bottom and top sides of the cTEG module. In order to better understand the realistic temperature gradient across the cTEG module, we use the finite element method (FEM) for temperature simulations. Figure 5 shows a thermal model of the as-produced cTEG with copper heat on the top and bottom sides. The module contains four pairs of TE legs with a size of 1 mm × 1 mm × 3.5 mm. The uniform heat transfer coefficient is set at 276 W/(m^2 K)

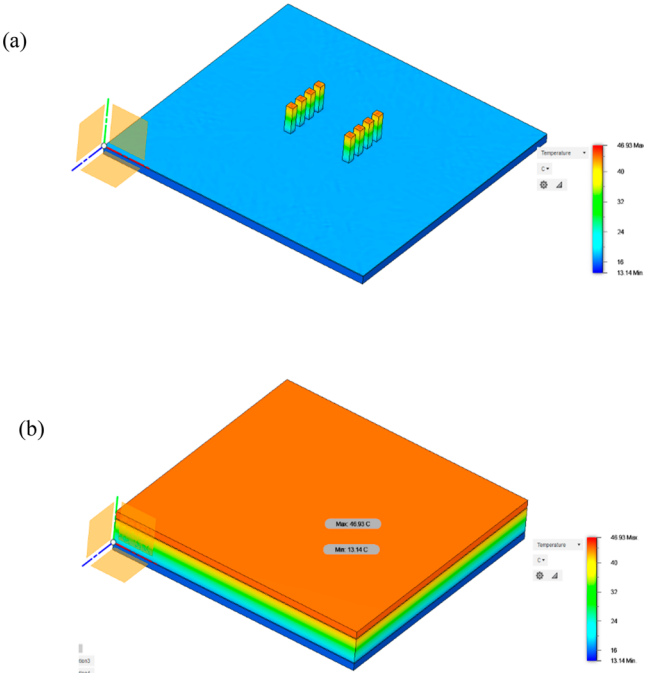

Figure 5. FEM simulation of the temperature profile for the cTEG with copper heat channels on the top and bottom sides, assuming that the uniform heat flux is applied. (a) Full assembly thermal model with four pairs of Bi_2Te_3 legs (1 mm × 1 mm × 3.5 mm) in the module. (b) Temperature results of the as-produced cTEG module.

https://doi.org/10.1021/acsaelm.1c00922
ACS Appl. Electron. Mater. 2022, 4, 197−205

and the mean water temperature is kept at T_{m_hot} = 53.3 °C and T_{m_cold} = 6.7 °C. The result shows a uniform distribution of heat on the substrate, and the temperature drops from the hot to the cold side.

As we discussed in a previous section on the electrothermal co-optimization of TEG device, it is necessary to match the electric load resistance with the internal resistance of the TEG module. The initial measured internal resistance of the cTEG at room temperature (25 °C) was 77 Ω. This was mainly attributed to the series resistance of the printed metal contact and the silver paste. As was previously discussed, the optimum power output can be achieved when the load resistance matches the internal resistance with the electrothermal interaction factor $\sqrt{1 + zT}$. In the experiment, the optimum load resistance can be found by manually changing the load resistance under a stable heat flow across the device.

The power output w at the load resistor is defined as[37]

$$w = \frac{R_L}{(R_L + R_{int})^2} V_{oc}^2 \quad (5)$$

where V_{oc} is the open circuit voltage from the TE module. Figure 6 shows the measured power output of the cTEG for

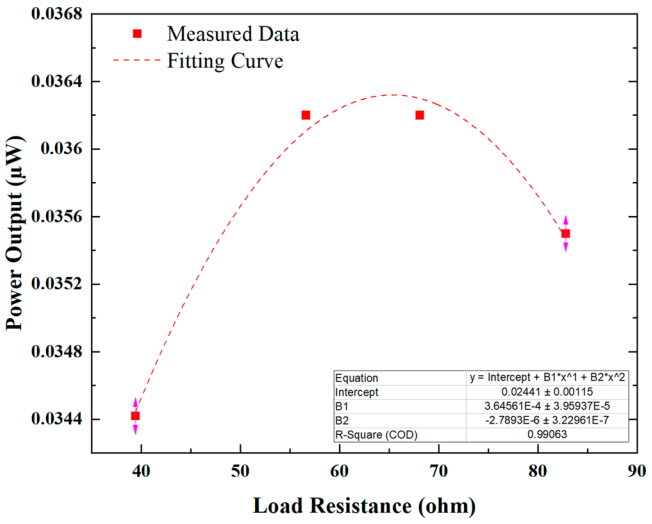

Figure 6. Experimental results and fitting curve for the power output as a function of load resistance at ΔT = 5 °C. The fitting curve uses a polynomial fitting function with intercept, B1, and B2 as shown in the inset table; the R^2 value is 99%.

ΔT = 5 °C against various load resistances. The power output of the cTEG increases as the load resistance increases. As the load resistance is near the internal resistance of the cTEG, the power output reaches a maximum value and then decreases when the load resistance is larger than the internal resistance. Thus, a series of experiments was repeatedly conducted to obtain the optimum power output by changes in the load resistance, as shown in Table 1. At ΔT = 5 °C, the optimized load resistance is found to be 56.6 Ω. The measured internal resistance at same temperature difference for the TE module is 60.1 Ω. The resistance will be affected by conditions such as temperature.

Figure 7 shows the measured load voltage and power output of the cTEG against the temperature difference between the

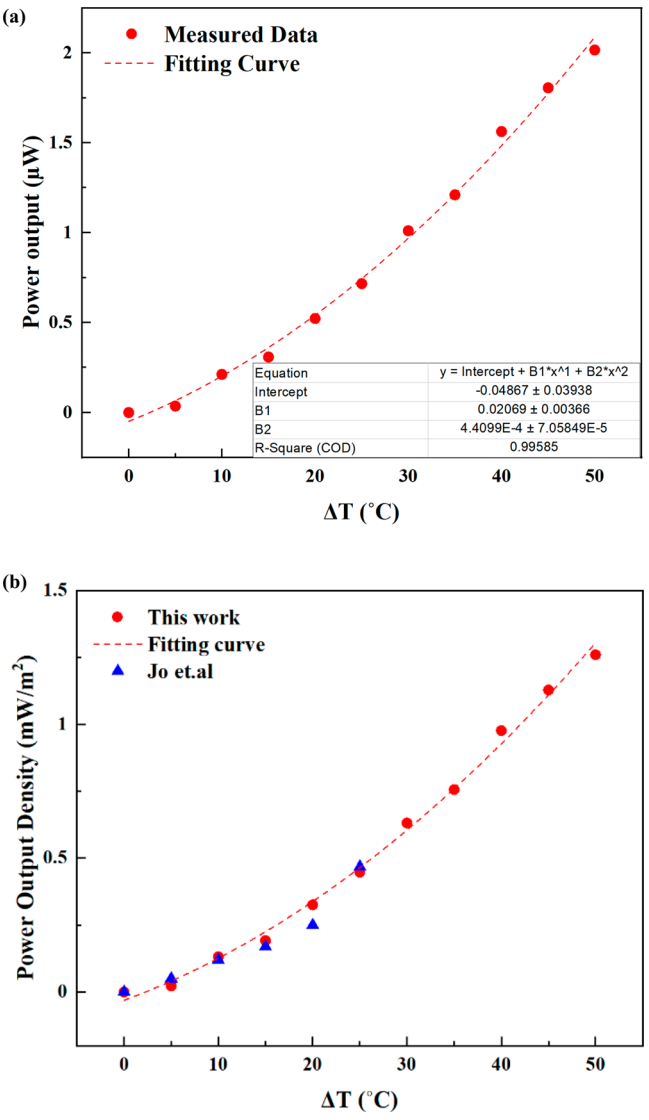

Figure 7. (a) Experimental results and fitting curve of power output as a function of temperature difference for the cTEG module with four pairs of TE legs in a 40 × 40 mm^2 substrate. The cold side is fixed at 5 °C. The fitting curve uses an exponential fitting function with an R^2 value of 99%. (b) Comparison of this work with that of Jo et al. on the power output density as a function of temperature difference. Both works follow the exponential trends.

Table 1. Internal Resistance, Optimized Load Resistance, and Maximum Power Output at Different Values of ΔT

	ΔT (°C)									
	5	10	15	20	25	30	35	40	45	50
internal resistance (Ω)	60.1	42.5	65.8	69	78.5	89.2	100	108	116.4	126.9
optimized load resistance (Ω)	56.6	39.4	68.1	68.1	82.8	82.8	100	100	120	120
max power output (μW)	0.04	0.21	0.31	0.52	0.72	1.01	1.21	1.56	1.81	2.02

https://doi.org/10.1021/acsaelm.1c00922
ACS Appl. Electron. Mater. 2022, 4, 197−205

top and bottom sides of the cTEG. The maximum power outputs at the matched load resistance were measured at various values of ΔT. The power output of the TE module increases with an increase in ΔT, and the power output value was 2.02 μW at ΔT = 50 °C.

At a low temperature difference, the power output densities are similar between this study and a previous study.[31] Jo et al. reported the power output density of the cTEG is 0.5 mW/m^2 at ΔT = 25 °C.[31] However, we obtained better performance at a higher temperature range; the maximum power output density of the prototype device in this study was 1.26 mW/m^2 at ΔT = 50 °C, as shown in Figure 7b. Theoretically, the more TE legs that are packed in the module, the the higher power output and voltage will be at a certain range of the fill factor.

The load voltage is also another essential parameter to evaluate device performance. It is important to have the cTEG generate sufficient voltage to satisfy the voltage requirement for IoT sensors or small electronics. In order to compare the load voltage with the expected load voltage, $V_{load,exp}$ is calculated as

$$V_{load,exp} = m/(1 + m) \times N_{leg} \times (S \times \Delta T) \quad (6)$$

where $m = \sqrt{1 + zT}$ is the optimum ratio of load resistance wtoith internal resistance, N_{leg} is the number of TE elements, and ΔT is the temperature across the cTEG module. Figure 8

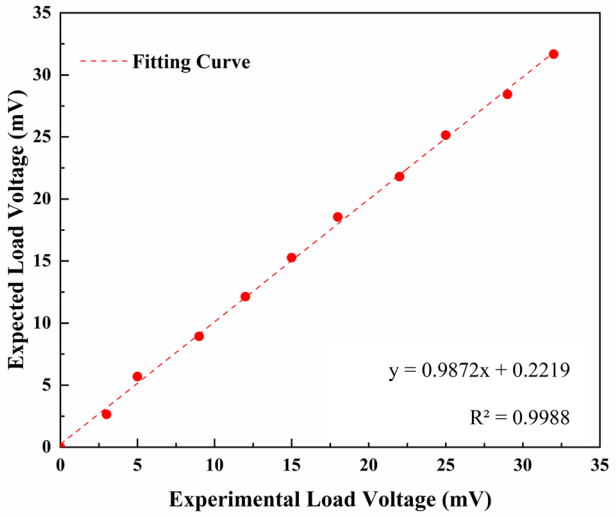

Figure 8. Fitting curve for load voltage comparison between experimental and simulation results. The fitting curve uses a linear fitting function with the intercept and slope shown in the inset table. A value of R^2 = 99% is obtained.

shows the relationship between the measured load voltage and the expected voltage. The results of the simulation are well matched with the experimental results. The fitting curve shows a linear function with R^2 = 99.88%, which indicates that the maximum load voltage is obtained at the optimum load resistance at each temperature range. The maximum load voltage is reached at 32 mV at 50 °C. The maximum voltage can be extrapolated as 44 mV if the temperature of the working fluid can be sustained at 200 °C. This voltage output can satisfy most low-power IoT sensor applications. For other applications which require a large voltage, one can connect a cTEG with a DC-DC booster to amplify the voltage output.

NUMERICAL ANALYSIS OF PERFORMANCE

Experimental Model. A numerical thermal analysis was conducted on the basis of the dimensions of the actual test sample described above. The simulation was used to understand whether the heat flow was properly given at the region of TE legs and went through the legs. The heat flux based on the device structure and boundary conditions defines the temperature gradients across the legs, and it is the direct component of power generation. Characterizing the heat flow through the relatively thin heterogeneous layers is a big challenge. Hence, a numerical simulation was used to understand the heat flow in this study.

The model consists of four pairs of p-type and n-type legs in the exact same footprint as the physical test sample device. The rest of the gap space in the TE module between two substrates made of a Kapton film[38] is filled with polydimethylsiloxane (PDMS). All the material properties in calculations are taken from the values at room temperature. The thermal boundary is defined with heat transfer coefficients, which are given at the midpoint temperature of the water flow (from chillers) on the hot and cold sides. The midpoint temperature is determined by the log mean temperature difference (LMTD) commonly accepted for the performance calculations of counterflow heat exchangers.

$$\mathrm{LMTD} = \frac{(T_{h,in} - T_{c,out}) - (T_{h,out} - T_{c,in})}{\ln(T_{h,in} - T_{c,out}) - \ln(T_{h,out} - T_{c,in})} \quad (7)$$

where the subscripts in and out stand for the inlet and outlet of the water flows, respectively.

The inlet temperature on the cold side is fixed at room temperature (25 °C), and the inlet temperature of the hot side is kept as a variable. The LMTD between the counterflow is used as the temperature difference between the hot side and cold side thermal baths. In this case, the module level heat energy regeneration by Joule heating is negligibly small, because the test sample has legs in only a fraction of the area. Similarly, Seebeck and Peltier effects created at the legs are small relative to the entire thermal conduction across the tested module. In the tested temperature range, TE properties are treated as temperature independent.

The heat transfer coefficient is calculated from the minichannel cold plate design specification using the equation

$$h = (A_{wet}/A_{base}) \times kNu/D_h \quad (8)$$

where A_{wet} is the wetted area of a single channel interim wall and A_{base} is the corresponding substrate area to the channel. This relation is correct as long as the thermal conductivity of the channel structure is high enough and there is no heat loss to the ambient air. The cross section of channels is square (0.5 mm × 0.5 mm) with 0.5 mm apart between channels. With an assumption of uniform heat flux, at the channel wall, the Nusselt number was given as 3.61 for a fully developed laminar flow according to Kays and London.[39] With the assumption that the heat loss factor is 75% to the other side and edges, the effective heat transfer coefficient applied to the test sample was calculated to be 276 W/(m^2 K).

The power output from the numerical model is calculated as the temperature at the hot contact T_h and the cold contact T_c to compare with experimental results. The external resistance is a design variable and is tested with various resistors in the experiment. A comparison plot (between simulation and

https://doi.org/10.1021/acsaelm.1c00922
ACS Appl. Electron. Mater. 2022, 4, 197−205

experiment) is shown in Figure 9, which reflects the maximum power output with optimum external load resistances.

$$W = \frac{R_L}{(R + R_L)^2}\{(T_h - T_c)S\}^2 \tag{9}$$

where

$$R = N_{leg}A_{leg}\frac{d}{\sigma} \tag{10}$$

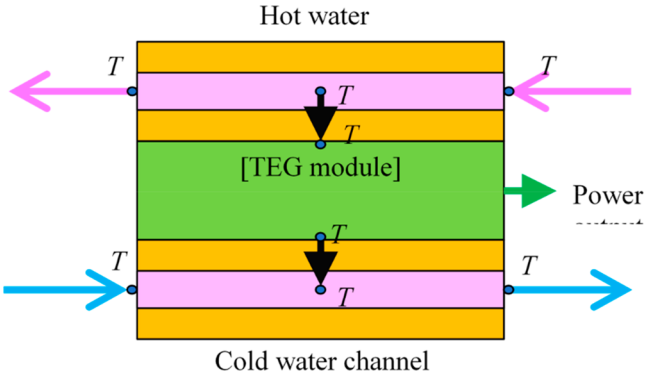

Figure 9. Schematic diagram of the counterflow temperature gradient in the hot and cold channels.

The series resistance of interconnects is also the design- and process-dependent factor that requires a careful investigation. Although this resistance will reduce the performance at the device level, we kept those unknowns out of the analyses since we wanted to make clear the theoretical maximum as the goal.

From the above, the TE properties at the maximum temperature are back-calculated from the output. These "effective" properties include all electrical and thermal losses across the cTEG module, and the values of these properties are clearly very different from those of the pure material properties. If the parameters are converted to per one leg, the conductivity can be found from experimental data using the equation

$$\sigma = \frac{d}{A_{leg}}\frac{1}{\left(\sqrt{\frac{V_{oc}^2}{W}R_L} - R_L\right)} \tag{11}$$

The Seebeck coefficient is simply found to be

$$S = \frac{V_{oc}}{LMTD} \tag{12}$$

and the thermal conductivity is found to be

$$k = \frac{Q_{leg}}{LMTD}\frac{d}{A_{leg}} \tag{13}$$

where Q_{leg} is determined by heat flow between hot and cold water per given area.

The Seebeck coefficient, electrical conductivity, and thermal conductivity are taken from the data for ΔT = 50 °C case as 85.8 μV/K, 221 S/m, and 5.37 W/(m K), respectively. Hence, the effective dimensionless zT is 4.03 × 10^{-3}. The large discrepancy from the standard bismuth telluride legs is due to the effective electrical conductivity, which is nearly 3 orders of magnitude smaller. The major reason is the parasitic series resistance, which may include contact resistance due to the inhomogeneous connection between the leg and the silver paint and some potential void inside the silver ink while it was cured.

The testing apparatus previously mentioned was designed to control the heat flow across the module; the heat transfer expected to a steam pipe in practical applications will differ from the above analyses. We calculated the practical heat transfer coefficients as 631 W/(m^2 K) on the steam convection side and 13.9 W/(m^2 K) for the air convection and radiation side. With the assumption that the fill factor is 20% for the leg to maintain practical manufacturability, the power output density for 200 °C steam and 27 °C air temperature with this module structure is calculated to be 1.2 mW/m^2. This value is certainly lower than that reasonably expected by extrapolating from the experimental result in Figure 7. The major difference comes from a 1 order of magnitude smaller convection heat transfer on the cold side, which limits the heat flux significantly.

If the contact and the contact resistance can be improved by 10^{-6} Ω/cm^2 and the electrical conductivity is that of the typical bismuth telluride, 1 × 10^5 S/m, this cTEG's potential power output density is predicted to 0.51 W/m^2 without a change in the Seebeck coefficient and thermal conductivity. From this analysis, a practical power generation can be predicted over 1 W/m^2 from a steam pipe by this cTEG.

CONCLUSIONS

The feasibility of a roll-to-roll cTEG manufacturing method was proved in a series of experiments and simulations that were designed to harvest waste heat from an underground pipeline system. A cTEG was integrated with four pairs of conventional p−n junctions and the silver metal patterns on the polyimide substrate laminated with PDMS as the filling gap was fabricated. The key value of this novel approach is prototyping a cTEG with bulk TE legs with flexible substrates in one step, which enables a significant cost reduction for a large-scale production. The device performance was tested by using a cold plate thermal boundary control with chillers for the hot and cold sides of the module. The results matched the predicted performance well and was 1.26 mW/m^2 for the case of ΔT = 50 °C. We extrapolated this data to a virtual case if the same legs were assembled in full arrays to implement on a steam pipe. The predicted performance was found to be 1.2 mW/m^2 if steam is 200 °C and the pipe is exposed to the ambient air of 27 °C. The limiting factors are poor air convection heat transport and the electrical parasitic resistance in the module. The results suggest that this novel manufacturing method can produce a cTEG with an energy of more than 1 W/m^2, enabling the cTEG to serve as a reliable and continuous power source for underground pipeline monitoring systems.

A 3D conjugate analysis was also conducted to identify the nonuniformity in temperature and heat flux. This helps to adjust the design of modules: e.g., p−n pair leg density, some variation of thickness, etc. The electrothermal optimization of a cTEG with an optimal heat path can result in the enhancement of device performance. In comparison to the current cTEG devices with a thickness of the TE leg in the micrometer range, the fabricated prototype in this study can combine TE legs with a millimeter range. This will ensure that all possible waste heat is harvested for power generation. Also, the roll-to-roll manufacturing process can simplify the fabrication method with low cost. This will enable the large-scale production for cTEGs to be used widely for powering

https://doi.org/10.1021/acsaelm.1c00922
ACS Appl. Electron. Mater. 2022, 4, 197−205

IoT sensors for underground pipeline monitoring to solve potential safety and environmental issues.

AUTHOR INFORMATION

Corresponding Author

Yining Feng − *Lyles School of Civil Engineering, Purdue University, West Lafayette, Indiana 47907, United States;* orcid.org/0000-0001-5683-0079; Email: feng109@purdue.edu

Authors

Kazuaki Yazawa − *Birck Nanotechnology Center, Purdue University, West Lafayette, Indiana 47907, United States;* orcid.org/0000-0002-6297-6290

Na Lu − *Lyles School of Civil Engineering, Purdue University, West Lafayette, Indiana 47907, United States; Birck Nanotechnology Center and School of Materials Engineering, Purdue University, West Lafayette, Indiana 47907, United States;* orcid.org/0000-0002-6367-1341

Complete contact information is available at: https://pubs.acs.org/10.1021/acsaelm.1c00922

Author Contributions

All authors contributed equally to this work.

Notes

The authors declare no competing financial interest.

ACKNOWLEDGMENTS

Y.F. and N.L. received funding from the National Science Foundation (NSF) under the program NSF 1560834. Y.F., K.Y., and N.L. received funding from the NSF under the program NSF 1919191.

REFERENCES

(1) Asbestos Confirmed in Steam Pipe That Exploded in Manhattan. The New York Times. https://www.nytimes.com/2018/07/19/nyregion/steam-explosion-pipe-flatiron-nyc.html (accessed April 26, 2021).

(2) Cheddadi, Y.; Cheddadi, H.; Cheddadi, F.; Errahimi, F.; Es-Sbai, N. Design and Implementation of an Intelligent Low-Cost IoT Solution for Energy Monitoring of Photovoltaic Stations. *SN Appl. Sci.* **2020**, *2* (7), 1−11.

(3) Han, G.; Su, Y.-F.; Nantung, T.; Lu, N. Mechanism for Using Piezoelectric Sensor to Monitor Strength Gain Process of Cementitious Materials with the Temperature Effect. *J. Intell. Mater. Syst. Struct.* **2021**, *32*, 1128−1139.

(4) Feng, Y.; Jiang, X.; Ghafari, E.; Kucukgok, B.; Zhang, C.; Ferguson, I.; Lu, N. Metal Oxides for Thermoelectric Power Generation and Beyond. *Adv. Compos. Hybrid Mater.* **2018**, *1* (1), 114−126.

(5) Tritt, T. M. Thermoelectric Phenomena, Materials, and Applications. *Annu. Rev. Mater. Res.* **2011**, *41* (1), 433−448.

(6) Zhou, C.; Ghods, A.; Saravade, V. G.; Patel, P. V.; Yunghans, K. L.; Ferguson, C.; Feng, Y.; Kucukgok, B.; Lu, N.; Ferguson, I. T. Review-The Current and Emerging Applications of the III-Nitrides. *ECS J. Solid State Sci. Technol.* **2017**, *6* (12), Q149−Q156.

(7) Qu, W.; Plötner, M.; Fischer, W. J. Microfabrication of Thermoelectric Generators on Flexible Foil Substrates as a Power Source for Autonomous Microsystems. *J. Micromechanics Microengineering* **2001**, *11* (2), 146−152.

(8) Hasebe, S.; Ogawa, J.; Toriyama, T.; Sugiyama, S.; Ueno, H.; Itoigawa, K. Design and Fabrication of Flexible Thermopile for Power Generation. In *MHS 2003-Proceedings of 2003 International Symposium on Micromechatronics and Human Science*; Institute of Electrical and Electronics Engineers: 2003; pp 287−291.

(9) Itoigawa, K.; Ueno, H.; Shiozaki, M.; Toriyama, T.; Sugiyama, S. Fabrication of Flexible Thermopile Generator. *J. Micromechanics Microengineering* **2005**, *15* (9), S233.

(10) Takashiri, M.; Shirakawa, T.; Miyazaki, K.; Tsukamoto, H. Fabrication and Characterization of Bismuth-Telluride-Based Alloy Thin Film Thermoelectric Generators by Flash Evaporation Method. *Sensors Actuators, A Phys.* **2007**, *138* (2), 329−334.

(11) Yadav, A.; Pipe, K. P.; Shtein, M. Fiber-Based Flexible Thermoelectric Power Generator. *J. Power Sources* **2008**, *175* (2), 909−913.

(12) Schwyter, E.; Glatz, W.; Durrer, L.; Hierold, C. Flexible Micro Thermoelectric Generator Based on Electroplated B1 2+xTe3-X. In *DTIP of MEMS and MOEMS-Symposium on Design, Test, Integration and Packaging of MEMS/MOEMS*; DTIP, 2008; pp 46−48.

(13) Glatz, W.; Schwyter, E.; Durrer, L.; Hierold, C. Bi2Te3-Based Flexible Micro Thermoelectric Generator with Optimized Design. *J. Microelectromechanical Syst.* **2009**, *18* (3), 763−772.

(14) Khan, S.; Dahiya, R. S.; Lorenzelli, L. Flexible Thermoelectric Generator Based on Transfer Printed Si Microwires. In *European Solid-State Device Research Conference*; IEEE Computer Society: 2014; pp 86−89.

(15) Hsiao, C. C.; Wu, Y. S. Fabrication of Flexible Thin-Film Thermoelectric Generators. *J. Chinese Inst. Eng. Trans. Chinese Inst. Eng. A* **2011**, *34* (6), 809−816.

(16) Delaizir, G.; Monnier, J.; Soulier, M.; Grodzki, R.; Villeroy, B.; Testard, J.; Simon, J.; Navone, C.; Godart, C. A New Generation of High Performance Large-Scale and Flexible Thermo-Generators Based on (Bi,Sb) 2 (Te,Se) 3 Nano-Powders Using the Spark Plasma Sintering Technique. *Sensors Actuators, A Phys.* **2012**, *174* (1), 115−122.

(17) Yang, Y.; Lin, Z. H.; Hou, T.; Zhang, F.; Wang, Z. L. Nanowire-Composite Based Flexible Thermoelectric Nanogenerators and Self-Powered Temperature Sensors. *Nano Res.* **2012**, *5* (12), 888−895.

(18) Im, H.; Moon, H. G.; Lee, J. S.; Chung, I. Y.; Kang, T. J.; Kim, Y. H. Flexible Thermocells for Utilization of Body Heat. *Nano Res.* **2014**, *7* (4), 443−452.

(19) Suemori, K.; Watanabe, Y.; Hoshino, S. Carbon Nanotube Bundles/Polystyrene Composites as High-Performance Flexible Thermoelectric Materials. *Appl. Phys. Lett.* **2015**, *106* (11), 113902.

(20) Francioso, L.; De Pascali, C.; Siciliano, P.; De Risi, A.; D'Amico, S.; Veri, C.; Pasca, M. Thin Film Technology Flexible Thermoelectric Generator and Dedicated ASIC for Energy Harvesting Applications. In *Proceedings of the 2013 5th IEEE International Workshop on Advances in Sensors and Interfaces, IWASI 2013*; IEEE, 2013; pp 104−107.

(21) Sevilla, G. A. T.; Inayat, S. B.; Rojas, J. P.; Hussain, A. M.; Hussain, M. M. Flexible and Semi-Transparent Thermoelectric Energy Harvesters from Low Cost Bulk Silicon (100). *Small* **2013**, *9* (23), 3916−3921.

(22) Fan, P.; Zheng, Z. H.; Li, Y. Z.; Lin, Q. Y.; Luo, J. T.; Liang, G. X.; Cai, X. M.; Zhang, D. P.; Ye, F. Low-Cost Flexible Thin Film Thermoelectric Generator on Zinc Based Thermoelectric Materials. *Appl. Phys. Lett.* **2015**, *106* (7), 073901.

(23) Navone, C.; Soulier, M.; Plissonnier, M.; Seiler, A. L. Development of (Bi,Sb) 2(Te,Se) 3-Based Thermoelectric Modules by a Screen-Printing Process. *J. Electron. Mater.* **2010**, *39* (9), 1755−1759.

(24) Lee, H. B.; We, J. H.; Yang, H. J.; Kim, K.; Choi, K. C.; Cho, B. J. Thermoelectric Properties of Screen-Printed ZnSb Film. *Thin Solid Films* **2011**, *519* (16), 5441−5443.

(25) Cao, Z.; Koukharenko, E.; Tudor, M. J.; Torah, R. N.; Beeby, S. P. Screen Printed Flexible Bi2Te3-Sb2Te 3 Based Thermoelectric Generator. *Journal of Physics: Conference Series* **2013**, *476*, 012031.

(26) Cao, Z.; Koukharenko, E.; Torah, R. N.; Tudor, J.; Beeby, S. P. Flexible Screen Printed Thick Film Thermoelectric Generator with Reduced Material Resistivity. *Journal of Physics: Conference Series* **2014**, *557*, 012016.

(27) Kim, S. J.; We, J. H.; Cho, B. J. A Wearable Thermoelectric Generator Fabricated on a Glass Fabric. *Energy Environ. Sci.* **2014**, *7* (6), 1959−1965.
(28) Kim, M. K.; Kim, M. S.; Jo, S. E.; Kim, H. L.; Lee, S. M.; Kim, Y. J. Wearable Thermoelectric Generator for Human Clothing Applications. In *2013 Transducers and Eurosensors XXVII: The 17th International Conference on Solid-State Sensors, Actuators and Microsystems, TRANSDUCERS and EUROSENSORS 2013*; IEEE, 2013; pp 1376−1379.
(29) Kim, M. K.; Kim, M. S.; Lee, S.; Kim, C.; Kim, Y. J. Wearable Thermoelectric Generator for Harvesting Human Body Heat Energy. *Smart Mater. Struct.* **2014**, *23* (10), 105002.
(30) Madan, D.; Wang, Z.; Chen, A.; Wright, P. K.; Evans, J. W. High-Performance Dispenser Printed MA p-Type Bi0.5Sb 1.5Te3 Flexible Thermoelectric Generators for Powering Wireless Sensor Networks. *ACS Appl. Mater. Interfaces* **2013**, *5* (22), 11872−11876.
(31) Jo, S. E.; Kim, M. K.; Kim, M. S.; Kim, Y. J. Flexible Thermoelectric Generator for Human Body Heat Energy Harvesting. *Electron. Lett.* **2012**, *48* (16), 1015−1017.
(32) Lu, Z.; Layani, M.; Zhao, X.; Tan, L. P.; Sun, T.; Fan, S.; Yan, Q.; Magdassi, S.; Hng, H. H. Fabrication of Flexible Thermoelectric Thin Film Devices by Inkjet Printing. *Small* **2014**, *10*, 3551−3554.
(33) Jiao, F.; Di, C. -a.; Sun, Y.; Sheng, P.; Xu, W.; Zhu, D. Inkjet-Printed Flexible Organic Thin-Film Thermoelectric Devices Based on p-and n-Type Poly(Metal 1,1,2,2-Ethenetetrathiolate)s/Polymer Composites through Ball-Milling. *Philos. Trans. R. Soc. A Math. Phys. Eng. Sci.* **2014**, *372* (2013), 20130008−20130008.
(34) Besganz, A.; Zöllmer, V.; Kun, R.; Pál, E.; Walder, L.; Busse, M. Inkjet Printing as a Flexible Technology for the Deposition of Thermoelectric Composite Structures. *Procedia Technol.* **2014**, *15*, 99−106.
(35) Bubnova, O.; Khan, Z. U.; Malti, A.; Braun, S.; Fahlman, M.; Berggren, M.; Crispin, X. Optimization of the Thermoelectric Figure of Merit in the Conducting Polymer Poly(3,4-Ethylenedioxythiophene). *Nat. Mater.* **2011**, *10* (6), 429−433.
(36) Yazawa, K.; Shakouri, A. Optimization of Power and Efficiency of Thermoelectric Devices with Asymmetric Thermal Contacts. *J. Appl. Phys.* **2012**, *111* (2), 024509.
(37) Yajima, T.; Tanaka, K.; Yazawa, K. Thermoelectric On-Spot Energy Harvesting for Diagnostics of Water Service Pipelines. In *Proceedings of the 17th InterSociety Conference on Thermal and Thermomechanical Phenomena in Electronic Systems, ITherm 2018*; Institute of Electrical and Electronics Engineers Inc.: 2018; pp 881−888.
(38) DuPont Kapton polyimide films: https://www.dupont.com/electronic-materials/kapton-polyimide-film.html (accessed January 5, 2021).
(39) Kays, W. M.; London, A. L. *Compact Heat Exchangers*; McGraw-Hill: 1984.

https://doi.org/10.1021/acsaelm.1c00922
ACS Appl. Electron. Mater. 2022, 4, 197−205